RESEARCH ARTICLE

Key Points:
- Background seepage contributes a steady surface flux of oil to the Gulf of Mexico
- The Deepwater Horizon discharge generated a dynamic surface slick of far greater size
- Response efforts coincided with decrease of floating volume, but increase in oil covered area

Supporting Information:
- Supporting Information S1
- Data Set S1
- Data Set S2A, S2B
- Movie S1

Correspondence to:
I. R. Macdonald,
imacdonald@fsu.edu

Natural and unnatural oil slicks in the Gulf of Mexico

I. R. MacDonald[1], O. Garcia-Pineda[1], A. Beet[2], S. Daneshgar Asl[1], L. Feng[3], G. Graettinger[4], D. French-McCay[5], J. Holmes[6], C. Hu[3], F. Huffer[1], I. Leifer[7], F. Muller-Karger[3], A. Solow[2], M. Silva[1], and G. Swayze[8]

[1]Florida State University, Dept. of Earth, Ocean, and Atmospheric Science, Tallahassee, Florida, USA, [2]Woods Hole Oceanographic Institution, Woods Hole, Massachusetts, USA, [3]University of South Florida, Dept. of Marine Science, St. Petersburg, Florida, USA, [4]NOAA OR&R, Seattle, Washington, USA, [5]RPS ASA, South Kingstown, Rhode Island, USA, [6]Abt Associates, Boulder, Colorado, USA, [7]Bubbleology Research International, Solvang, California, USA, [8]U.S. Geological Survey, Lakewood, Colorado, USA

Abstract When wind speeds are 2–10 m s^{-1}, reflective contrasts in the ocean surface make oil slicks visible to synthetic aperture radar (SAR) under all sky conditions. Neural network analysis of satellite SAR images quantified the magnitude and distribution of surface oil in the Gulf of Mexico from persistent, natural seeps and from the Deepwater Horizon (DWH) discharge. This analysis identified 914 natural oil seep zones across the entire Gulf of Mexico in pre-2010 data. Their $\sim$0.1 μm slicks covered an aggregated average of 775 km^2. Assuming an average volume of 77.5 m^3 over an 8–24 h lifespan per oil slick, the floating oil indicates a surface flux of 2.5–9.4 $\times$ 10^4 m^3 yr^{-1}. Oil from natural slicks was regionally concentrated: 68%, 25%, 7%, and <1% of the total was observed in the NW, SW, NE, and SE Gulf, respectively. This reflects differences in basin history and hydrocarbon generation. SAR images from 2010 showed that the 87 day DWH discharge produced a surface-oil footprint fundamentally different from background seepage, with an average ocean area of 11,200 km^2 (SD 5028) and a volume of 22,600 m^3 (SD 5411). Peak magnitudes of oil were detected during equivalent, $\sim$14 day intervals around 23 May and 18 June, when wind speeds remained <5 m s^{-1}. Over this interval, aggregated volume of floating oil decreased by 21%; area covered increased by 49% ($p < 0.1$), potentially altering its ecological impact. The most likely causes were increased applications of dispersant and surface burning operations.

1. Introduction

A thin layer of petroleum floating on the ocean came to be called an oil slick because it suppresses surface roughness. The resulting reflective contrasts in the ocean surface make oil slicks visible to passive remote sensing under clear daylight skies [*Fingas and Fieldhouse*, 2012; *Hu et al.*, 2009; *MacDonald et al.*, 1993], and to synthetic aperture radar (SAR) under all sky conditions [*Brekke and Solberg*, 2005; *Fingas and Fieldhouse*, 2012; *Leifer et al.*, 2012]. The volume of oil floating on the ocean surface decreases due to evaporation, photooxidation, dissolution, entrainment (mixing into the water column), and microbial oxidation; as a result, an oil slick will become progressively less visible and disappear over time [*Reed et al.*, 1999]. Therefore, oil slicks repeatedly observed in similar localities are a robust indication that oil discharge from natural sources or pollution is ongoing [*Daneshgar Asl et al.*, 2015; *MacDonald et al.*, 1996]. In this study, we used satellite SAR to quantify surface oil released from natural seeps across the Gulf of Mexico and from the Deepwater Horizon (DWH) discharge of 2010.

Natural seeps are broadly distributed across the Gulf of Mexico [*De Beukelaer et al.*, 2003; *MacDonald*, 2011], with oil discharge rates from individual natural seeps thought to be generally <1 m^3 d^{-1} [*National Research Council Committee on Oil in the Sea*, 2003]. Satellite SAR can readily detect these oil slicks under favorable wind conditions, i.e., speed 2–10 m s^{-1} [*Espedal and Wahl*, 1999]. In the 1990s and early 2000s, a provisional remote sensing inventory indicated that natural oil slicks cover an average aggregate footprint of 850 km^2 on the Gulf at any given time [*Mitchell et al.*, 1999], from which the annual discharge rate for the entire Gulf was estimated to be 0.38–1.0 $\times$ 10^5 m^3 yr^{-1} or 2.5–6.9 $\times$ 10^5 bbl yr^{-1} and natural seeps were cited as the predominant source of oil entering the ocean [*Mitchell et al.*, 1999; *National Research Council Committee on Oil in the Sea*, 2003]. Subsequent to the DWH discharge, several authors have noted the prevalence of

natural seeps in the vicinity of the DWH wreck [*Crooke et al.*, 2015], the challenge of distinguishing natural oils slicks from anthropogenic releases [*Aeppli et al.*, 2013; *Garcia-Pineda et al.*, 2015], and the possibility that oil from natural seeps causes deleterious impact to deep sea fauna [*Boehm and Carragher*, 2012] comparable to that attributed to oil from the DWH discharge [*White et al.*, 2012]. The present work updates and refines estimates for the number, distribution, and output rates of natural seeps in the Gulf of Mexico. This can provide a basis for evaluating the fate and effect of oil from chronic background sources versus oil from large, but transient anthropogenic discharges.

In contrast to the widespread background seepage, the DWH event released $\sim 10^5$ m^3 d^{-1} from a single damaged well in 1500 m water depth [*McNutt et al.*, 2011]. A fraction of the DWH discharge was dispersed in deep-ocean plumes [*Camilli et al.*, 2010; *Ryerson et al.*, 2011] with some coming to rest on the ocean floor [*Chanton et al.*, 2015; *Valentine et al.*, 2014]. Oil that reached the surface spread across thousands of km^2 of the ocean [*Lubchenco et al.*, 2012], while natural oil weathering processes and strenuous response efforts to control the discharge influenced the magnitude and fate of the floating oil [*Lehr et al.*, 2010; *Leifer et al.*, 2012; *McNutt et al.*, 2011; *Ryerson et al.*, 2011].

By examining changes in the amount of oil detected on the ocean surface with satellite SAR, we quantify the extent, magnitude, and movement of DWH oil. Remote sensing data have been used to investigate the DWH discharge based on limited numbers of optical [*Bulgarelli and Djavidnia*, 2012; *Hu et al.*, 2011; *Maianti et al.*, 2014; *Svejkovsky et al.*, 2012] and SAR images [*Garcia-Pineda et al.*, 2013a; *Lubchenco et al.*, 2012; *Marghany*, 2014]. No previous study has had the opportunity to analyze a comprehensive collection of remote sensing data, which covered the entire impacted region from beginning to end of the emergency, with use of consistent, objective methods. We compared SAR results to changing rates of oil discharge, response treatment that included aerial and subsea application of dispersants, and controlled burning of surface oil that have been reported in publically available records [*Houma ICP Aerial Dispersant Group*, 2010; *Lehr et al.*, 2010; *Mabile and Allen*, 2010]. The results from the DWH discharge shed light on the fate of the surface oil as well as the effects of different response efforts and environmental conditions. Comparison of the chronic natural supply to acute oil pollution events using consistent methodology can provide results that inform ongoing research on impacts of hydrocarbons in a marine basin.

2. Materials and Methods

2.1. SAR Images

This study is based upon two separate collections of SAR data that were acquired over the Gulf of Mexico under conditions suitable for detecting floating oil. To quantify oil discharged from natural seeps, we reviewed 1158 prospective images obtained through the Alaska Satellite Facility (ASF) and analyzed 254 individual SAR images collected by the Radarsat-1, JERS-1, and ERS1 satellites between May 1997 and November 2007. Note that SAR images, as they are cataloged in the ASF archive, can overlap along the data acquired during an orbital pass of a satellite. Combining frames that overlapped along individual orbital paths yielded a total of 176 distinct SAR acquisitions (supporting information Table S1).

All data were converted from Level1 format to 8 bit geotiff with use of the MapReady software from ASF. Images were chosen for analysis with the objective to obtain complete and replicated sampling of the entire Gulf of Mexico, with higher replication in regions known to host natural seeps, and to utilize images obtained under sea conditions that were compliant with detection of floating oil. Proportional sampling density for this image collection covering the entire Gulf of Mexico was compiled as 10 km gridded values in geographic projection. On average, each grid cell was sampled 15.3 times; cells with zero samplings were restricted to bay and near-coastal areas where natural seeps are not known to occur (supporting information Figure S1).

To quantify the distribution of floating oil during the discharge from the DWH, we analyzed 166 SAR images collected by Radarsat-1, Radarsat-2, TerraSAR-X, CosmoSKY-MED 1-2-3-4, ENVISAT, ALOS-1, and ERS-2 satellites between 23 April 2010 and 2 August 2010. Data were obtained in a wide range of formats, including N1 (Envisat), Level1, geotiff 8 bit, and geotiff 16 bit. Rendering of raw satellite data to 8 and 16 bit geotiff formats was performed using a range of brightness and contrast settings. To maximize the revisit coverage over the spill, each satellite had to adjust and reaim the viewing beam mode each time an image was acquired. The resulting images varied in terms of resolutions, incidence angles, and polarizations,

summarized in the supporting information Table S2. To estimate the contribution of thicker patches of floating oil to the aggregated volume, a subset of the SAR images collected during the DWH discharge was additionally analyzed to detect small SAR image anomalies caused by thicker patches of emulsion within overall regions of floating oil with use of the Oil Emulsion Detection Algorithm (OEDA) [*Garcia-Pineda et al.*, 2013a]. A total of 60 SAR images that detected the floating oil were analyzed for this purpose. The satellite images and resulting data sets that were gridded for input are cataloged in supporting information Table S3.

2.2. Environmental Data and DWH Response Effects

The determination that each SAR image was obtained when wind speeds were compliant with detection of floating oil was based on ocean buoy data, modeled wind products, and visual evaluation of image texture. Modeled wind time series were obtained from the NAM ocean model [*Janjic et al.*, 2010], realized in 6 h time steps on a 5 × 5 km grid for analysis of DWH oil. The 5 km grid used for the DWH results conformed to the NRDA DWH Albers grid. Daily magnitude and spatial distribution of aerial dispersant application [*Houma ICP Aerial Dispersant Group*, 2010] and burning operations [*Mabile and Allen*, 2010] were obtained from publicly available databases. Daily discharge and recovery rates as well as daily subsea dispersant injection quantities were taken from the Oil Budget Calculator [*Lehr et al.*, 2010].

Sea level observations of floating oil from the DWH discharge included surprisingly few physical collections, but many qualitative observations [*NOAA Hazmat*, 2012], that were used to corroborate presence or absence of floating oil, and occurrence of thicker layers of emulsified oil based on the color and appearance of floating oil [*Garcia-Pineda et al.*, 2013a]. Locations of natural seeps were checked against published results [*Brooks et al.*, 1990; *Garcia-Pineda et al.*, 2010; *MacDonald et al.*, 1996; *Roberts and Boland*, 2010] and reports from recent expeditions.

2.3. SAR Image Processing: Presence-Absence of Oil

After preliminary processing, SAR images were analyzed for presence of floating oil with use of the Texture Classifying Neural Network Algorithm (TCNNA), which has been described in previous publications [*Garcia-Pineda et al.*, 2010, 2013b, 2009]. This semiautomated routine filters a gray scale image with a 25 × 25 pixel kernel, testing pixel-by-pixel for edge and shape detections based upon the Leung-Malik filter bank [*Leung and Malik*, 2001]. The neural network algorithm interpolates these detections within a training set previously compiled by an expert operator through classification of several thousand pixels in images known to contain natural oil slicks, which are distinctive linear features, broadest near the origin and tapering away down-wind. Training sets were also compiled for the floating oil targets resulting from the DWH discharge, which were much larger in area and contained a greater variety of regular and irregular shapes. Detection of floating oil with TCNNA was repeatedly validated by comparison with sea level observation.

Under local conditions of low or zero wind, substantial regions of an image would appear radar-dark in the absence of capillary waves on the ocean surface. Low-wind regions were recognizable as contiguous features lacking patchiness caused by uneven distributions of floating oil. Regions of antenna pattern noise, rain cells, or low wind were carefully masked off from the surrounding image features to avoid false-positive classifications and were classified as no-data regions of the image (e.g., supporting information Figure S3). Resolution of individual pixels depended upon the satellite and collection mode, but was generally in the range 25–100 m.

2.4. SAR Image Processing: Emulsion Anomalies

A separate algorithm was employed to detect small regions of emulsified oil within the large oil slicks generated by the DWH discharge. The Oil Emulsion Detection Algorithm (OEDA) was developed based on the unprecedented number of remote sensing collections completed during the emergency, specifically near-synoptic observations with different sensors and sea level validation by responders [*Garcia-Pineda et al.*, 2013a]. The numerical approach described by these authors required evaluating the 16 bit SAR images with the use of a satellite-specific normalization polynomial. This procedure detected small regions (<2% of total oil slick area), where oil emulsion produced a scattering effect that was intermediate between the high, radar-bright backscatter from clean sea and the radar-dark areas where floating oil suppressed capillary waves. Features extracted using this procedure were consistent in size, location, and time with observations from other optical and hyperspectral sensors, as well as from direct observations at sea level [*Garcia-Pineda et al.*, 2013a]. The approach was applicable for 60 of the 166 SAR images used in the DWH portion of this

study. Images were chosen for analysis which were free from rain cells or low-wind regions, and analysis was restricted to the sectors of the images where the scan angle was in the range of about 20°–50°. All images used for OEDA analysis are identified in supporting information Table S3. Despite the paucity of physical collections of floating oil, there were many qualitative observations that could be used to corroborate presence or absence of floating oil and occurrence of thicker layers of emulsified oil, and which showed significant correlation to emulsified oil detected by the OEDA analysis [*Garcia-Pineda et al.*, 2013a].

Determining an accurate scalar for the volume of oil that comprised layers of emulsion utilized two lines of evidence. Hyperspectral data found that oil slick thickness during the DWH discharge ranged from 0.1 μm to >100 μm, with patches on the order of up to 1000 μm possible [*Lehr et al.*, 2010]. The SAR data were able to detect floating oil across this entire range with Texture Classifying Neural Network Algorithm, with thick emulsions identified as anomalies [*Garcia-Pineda et al.*, 2013a]. The mean thickness of these anomalies was determined from statistics of oil slick volume estimates of the DWH spill on 17 May 2010 using measurements by the hyperspectral Airborne Visible/Infrared Imaging Spectrometer (AVIRIS) and a spectral matching algorithm after atmospheric correction [*Clark et al.*, 2010]. The 7.6 m resolution AVIRIS data were binned to 30 m (comparative to SAR resolution) to calculate the cumulative occurrence frequency, with the upper inflection point estimated to be about 70 μm (supporting information Figure S2) [*Sun et al.*, 2015].

An independent estimate of oil thickness was obtained from the burning operations, which typically collected oil from over several square km of ocean area [*Mabile and Allen*, 2010]. Taking the reported volume of oil burned in 365 operations, divided by the ocean area from which it was reported to have been collected, indicates that oil of sufficient volume to be collected for burning had an average thickness of 72 μm (SD 4.64). On the basis of the AVIRIS results and the reports from the burning operations, we specify a ∼70 μm thickness for oil anomaly pixels identified by OEDA [*Garcia-Pineda et al.*, 2013a]. All other oil-covered regions were classified as "sheen." The thickness of such classified "sheen" was set at ∼1 μm following published standards [*ASTM International*, 2006; *NOAA Hazmat*, 2012].

2.5. Gridded Data Sets

The TCNNA processing of a SAR image yielded a set of pixels (typically ∼100 × 100 m) that were classified as oil-covered water. These pixels were aggregated as gridded data. A 10 × 10 km geographic grid was used for the natural seep data. An Albers equal area grid was used for the DWH study, conforming to the National Resource Damage Assessment DWH study grid (5 × 5 km). Output from OEDA analysis included a third variable: the proportion of oil-covered water containing thick emulsions. Grid cells that were partially sampled by an image, or that contained no-data regions due to low wind or noise, were not included in the output. The same grid was used to localize the aerial dispersant applications and controlled burning operations, as well as output of the NAM wind model.

2.6. Analysis of Natural Oil Seep Zones

The set of SAR images taken from 176 distinct SAR acquisitions were found to contain possible oil slicks somewhere within the sampled area (supporting information Table S1). An oil slick origin (OSO) was defined as the localized region where a rising stream of oil droplets arrives at the surface [*Garcia-Pineda et al.*, 2010]. An oil slick from a natural seep is the elongated film that drifts away from an OSO with movement of surface water [*De Beukelaer et al.*, 2003]. Over a period of ∼10–20 h, an OSO location is more or less fixed, while the shape and length of its slick depend on wind direction and speed [*MacDonald et al.*, 2002]. The end of an oil slick is the point beyond which the floating film has dissipated so that it no longer produces wave damping effects that can be distinguished by remote sensing. Natural seep zones produce one to several such streams, discharging from discrete vents on the seafloor. Over periods of days or longer, the surface location of an OSO will change relative to its seafloor vent as midwater currents displace vertical pathways to the surface. Our analysis of natural seeps with TCNNA processed SAR images had the following goals: (1) identify individual or clusters of OSO features in SAR images produced from geologic seep zones, (2) compare the locations of OSO clusters across multiple SAR images to pinpoint active seep zones, and (3) quantify the areal extent of floating oil from natural slicks. The detailed methods for goals 1 and 2 have been described in a previous publication and are briefly recapitulated below [*Garcia-Pineda et al.*, 2010].

2.7. Surface Oil From Natural Seeps

To determine the clustering scale for active seep zones, we compared all pairwise distances among 100 OSO features in SAR images taken over an identical region of the north-central Gulf of Mexico. The distance increased gradually in the range of about 100–2000 m and abruptly beyond 2500 m pairwise-distance. We interpret this inflection as the shift that occurs between vents within an active seep and vents associated with a distinct geologic structure. Accordingly, for an individual SAR image, we identified seep zones by taking the geographic centroid of vents clustered within diameters of <2500 m. In some cases, these zones could be pinpointed by seafloor observation from submersibles [*De Beukelaer et al.*, 2003; *Garcia-Pineda et al.*, 2010; *MacDonald et al.*, 1996, 2003]. Where such exploration was not available, multiple observations of OSO clusters were required to eliminate the possibility of false positives or transient events. However, the density of active seep zones is high in the Gulf, so a means to group OSO clusters when comparing among multiple images is needed. Working from the locations of known seep zones, we found an empirical linear relationship (least squares $R^2 = 0.925$) between water depth and the deflection between a vent and its OSO:

$$X = 1.2346Z + 796.86 \tag{1}$$

where X (m) is the lateral displacement between an OSO and its seafloor vent location, and Z is water depth (m). Derivation of this relationship has been described in an earlier publication [*Garcia-Pineda et al.*, 2010]. Applying this relationship to clusters of OSO centroids was the method by which we identified possible seep zone locations in unexplored regions.

To estimate the average amount of oil-covered water resulting from natural seepage in the Gulf of Mexico, each TCNNA-processed SAR image was considered a separate, independent sample of an arbitrary size from the offshore area. An estimate of the mean area of oil-covered water was obtained by summing the mean area covered in each of the individual grid cells, which for any given cell was found by averaging over those of the 176 SAR acquisitions which contained that cell. Similar procedures led to estimates for different regions and for differences between quadrants. Standard deviations for these estimates were obtained by bootstrapping [*Chernick*, 1999]. Estimates were computed for 100,00 bootstrap samples consisting of 176 images sampled with replacement from the original 176 SAR acquisitions, and the standard deviation of these 10,000 estimates is reported. This bootstrap methodology is justified if the original 176 SAR acquisitions may be regarded as a random sample from a hypothetical infinite population of such images. The procedure allowed for the estimation of standard error and for statistical comparison of different subregions of the Gulf of Mexico.

2.8. Interpolation Method for Surface Oil From DWH

To interpolate among the SAR images that detected surface oil during DWH, we used the following algorithm: let the random variable $Y_j(t)$ be the area of cell j that is covered by oil at time t. The basic statistical assumption is that $Y_j(t)$ is the sum of a time-varying mean $\mu_j(t)$ and a random error with mean of zero and spatial covariance function:

$$Cov(Y_j(t), Y_k(t)) = \sigma^2 \exp(-\theta d_{jk}) \tag{2}$$

where d_{jk} is the distance between the centers of cells j and k. The total area covered by oil at time t is $Y(t) = \sum_j Y_j(t)$ where the sum is over all cells. The mean and variance of $Y(t)$ are:

$$\sum_j \mu_j(t) \text{ and } \sigma^2 \sum_j \sum_k \exp(-\theta d_{jk}), \text{ respectively} \tag{3}$$

To estimate these quantities, it is necessary to estimate $\mu_j(t)$ for all j and t and the covariance parameters σ^2 and θ. The estimate of $\mu_j(t)$ is given by:

$$\hat{\mu}_j(t) = \frac{\sum_k w_k Y_j(t_{jk})}{\sum_k w_k} \tag{4}$$

where the sum is over the times t_{jk} at which cell j was observed, $Y_j(t_{jk})$ is the observed area covered in cell j at time t_{jk}, and the weight w_k is given by:

$$w_k = \exp\left(-(t - t_{jk})/h\right)^2 \tag{5}$$

where h is a bandwidth parameter chosen to be 48 h based upon minimizing mean squared error that was found. The TCNNA results for individual SAR images were compared iteratively to estimates obtained by interpolating among all remaining images.

The covariance parameters were estimated by forming the variogram of the cross-validation residuals $Y_j(t_{jk})$ $-\tilde{\mu}_j(t_{jk})$ where $\tilde{\mu}_j(t_{jk})$ is the kernel estimate of $\mu_j(t_{jk})$ omitting the observed value $Y_j(t_{jk})$. These residuals were formed for each observation time and then pooled to form the variogram. The variogram is a standard measure of spatial correlation that is related closely to the spatial covariance function. The covariance parameters were estimated by the weighted least squares method of Cressie [*Cressie*, 1991]. The assumption that the pattern of spatial covariance is independent of time was confirmed from the similarity of variograms for the separate observation times.

The same procedure was used to estimate the area covered by thick oil and to characterize uncertainty in it. The error bound for the combined volume of oil was calculated by combining the uncertainty terms for thin and thick oil and applying 1 and 70 μm scalars for area and thickness. The interpolation method outlined above was used to predict coverage of oil and thick oil in each cell to compile maps of DWH surface oil concentrations from all available images and all cells in which oil was detected (supporting information Database S2A). The same procedure was used to estimate total magnitudes of surface oil at regular intervals. For these calculations, the overall region of prediction was restricted to the set of cells for which the largest gap between prediction time and an observation was less than 9 days (supporting information Database S2B). This ensured that prediction was local in time.

3. Results

3.1. Gulf of Mexico Natural Oil Seeps

Satellite remote sensing data have previously been used to compile inventories of persistent background oil sources in the present-day Gulf of Mexico and to thereby quantify a pathway by which fossil carbon reenters the living Earth system [*MacDonald et al.*, 1996; *National Research Council Committee on Oil in the Sea*, 2003]. We used the Texture Classifying Neural Network Algorithm (TCNNA) to analyze 176 SAR images (supporting information Figure S1) collected over the Gulf prior to 2010. Slicks that clustered in restricted localities among multiple images indicated the occurrence of seabed seep zones, which were controlled by the geologic features that allow hydrocarbons to escape into the water column from subsurface reservoirs through faults [*Abrams*, 2005; *Garcia-Pineda et al.*, 2010; *Whelan et al.*, 2005].

The analysis identified 914 distinct seep zones (Figure 1 and supporting information Database S1), which are concentrated in a north to south trend from the Texas-Louisiana Slope. They trend through the Sigsbee Knolls and the Campeche Knolls [*Bryant et al.*, 1991], to a cluster of sources that occur within the supergiant Cantarell Complex oil field on the Campeche Bank of the Yucatan Peninsula [*Miranda et al.*, 2004]. Oil slicks or similar features were eliminated from the inventory when no seep zone was observed within its 10 km grid cell and a one-cell buffer surrounding that cell. This filter removed anomalies that were detected in solitary SAR images. Integration of multiple images predicts the seafloor locations of persistent natural oil seeps. Geographically, the largest numbers of seeps are associated with the salt-tectonic stratigraphy of the Gulf of Mexico, which is most pronounced in the central and western region of the continental slope [*McBride et al.*, 1998; *Watkins et al.*, 1978]. There was progressive curtailment of natural discharges detected by SAR eastward along the Mississippi-Alabama Slope in the direction of the Florida Platform, a massive carbonate structure where sediment accumulation has been limited during basin history and salt bodies are absent [*Hine et al.*, 2003; *Pindell and Kennan*, 2007].

The average area of TCNNA-detected surface oil was compiled as a 10 × 10 km gridded data set to show the average proportion of surface waters covered by background oil discharges (Figure 2). This analysis did not include gas vents or mud volcanoes that discharged insufficient oil to create a surface slick or transient discharges that were not detected across multiple SAR images. Although persistent pollution is a component in the background discharge of surface oil in the Gulf of Mexico [*Daneshgar Asl et al.*, 2015; *Miranda et al.*, 2004], the distribution of source locations indicates that the majority of this oil comes from natural seeps [*De Beukelaer et al.*, 2003; *Garcia-Pineda et al.*, 2010; *MacDonald et al.*, 1993, 2004, 1996].
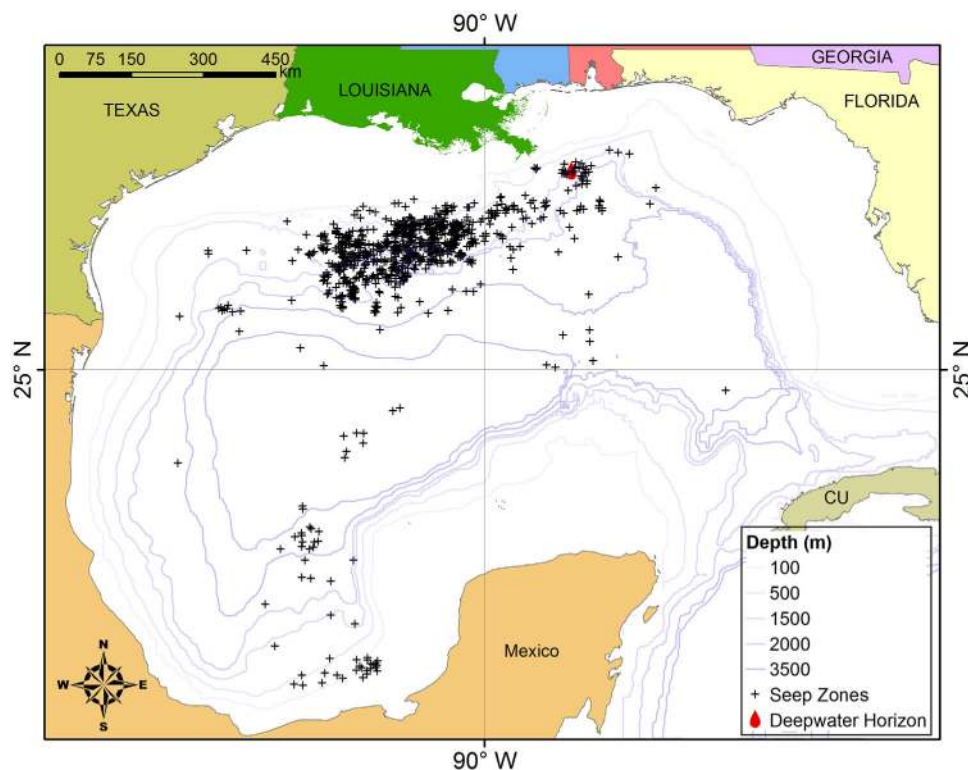
Figure 1. Natural seep zones in the Gulf of Mexico. Each point is the geographic average of oil slick origins discharged from a discrete geologic seep approximately 2 km in diameter. Estimated total active seep zones total 914 locations.

Surface slicks exhibit unusual characteristics compared with other ocean features detected by remote sensing. Their two-dimensional area can cover many square kilometers of ocean surface, yet they have a thickness measured in microns. Determining the volume of oil required to form a slick depends upon approximations of slick thickness that are inherently difficult to verify. The maximum average area of floating oil in a 10 × 10 km grid cell was 15 km^2, but the oil-covered area per cell was typically much smaller. Following methods previously used to estimate the total flux of natural oil to the surface of the Gulf of Mexico [*MacDonald et al.*, 1993; *National Research Council Committee on Oil in the Sea*, 2003], we estimate that the average thickness of natural oil slicks is ∼0.1 μm. Using this scalar, the area of persistent natural oil slicks can be expressed as volume per area (m^3 km^{-2}), which will enable comparison with anthropogenic events such as the DWH discharge (Figure 2).

Division of the Gulf into four subregions along lines of 25°N latitude and 90°W longitude provides a basis for comparing the scale of oil seepage in the northwest, northeast, southeast, and southwest portions of the basin (Figure 2 and supporting information Database S1). The four subregions each comprise from 16% to 34% of the Gulf's total 1,473,700 km^2 area. The northwestern subregion, encompassing most of the Texas-Louisiana Slope and Sigsbee Escarpment areas, was the largest source of floating oil in the Gulf; it contributed an average of 68% of the total. The southwestern subregion, containing the Cantarell field and the Campeche Knoll seeps [*MacDonald et al.*, 2004], contributed an average of 25% of the total. The northeastern subregion, including Mississippi Canyon, where the Deepwater Horizon incident occurred, contributed only 7% of the background oil seepage into the Gulf of Mexico (Table 1 and supporting information Database S1).

The maximum mean volume of surface oil from natural oil seeps in a grid cell was 0.015 m^3 km^{-2} (0.09 bbl km^{-2}) (Figure 2). The combined footprint of all natural oil slicks, based on average oil cover per grid cell, is 779 km^2 (SD 86.24). These microscopically thin oil layers rarely survive more than 8–24 h on the ocean surface before evaporation and dispersion remove them as coherent features in remote sensing data [*De Beukelaer et al.*, 2003; *MacDonald et al.*, 2013]. Taking these time constants as the formation rate for the composite area of natural slicks, the annual discharge from seeps for the entire Gulf equates to a flux at the
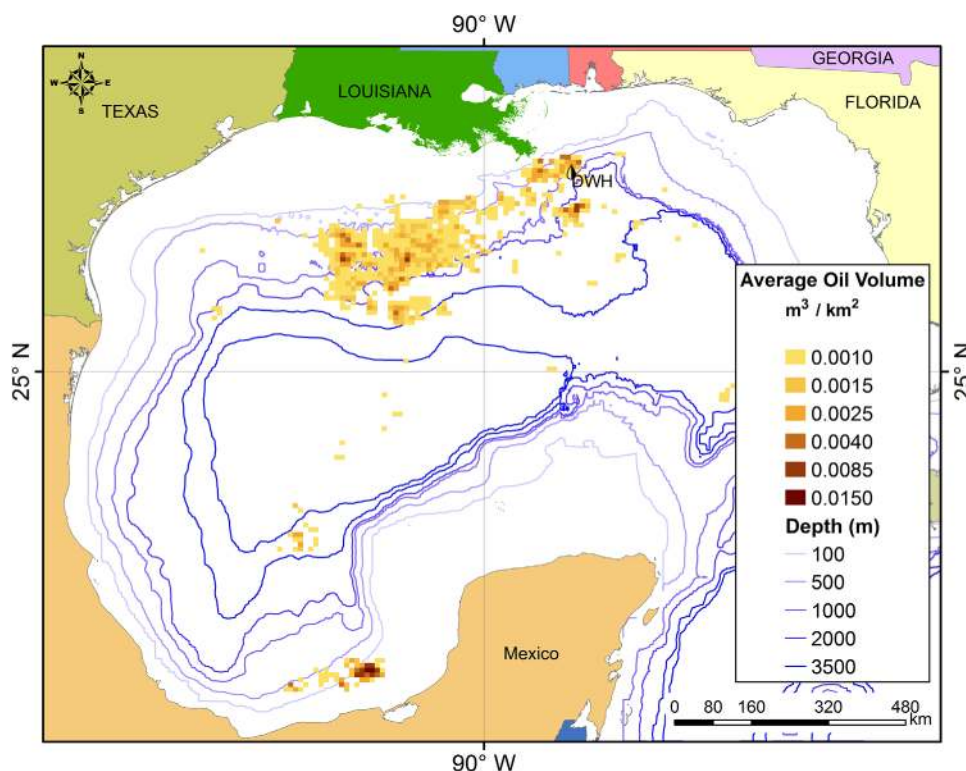
Figure 2. Map of natural oil slick sources: abundance and distribution of persistent surface oil in the Gulf of Mexico. Values for average surface volume (m³ km⁻²) gridded at 10 km × 10 km scale. Sources of this oil are 914 natural seep zones.

sea surface of $2.51–9.43 \times 10^4$ m³ yr⁻¹ ($1.58–5.94 \times 10^5$ bbl yr⁻¹). Similar calculations can be performed for each of the four Gulf subregions (Table 1). These estimates are in reasonable agreement with previous results, but are presented with statistically defined error bounds and subregional resolution.

3.2. Spatial Distribution of DWH Surface Oil

To investigate the magnitude and distribution of surface oil discharged by DWH, we adapted the TCNNA process used for background seeps to analyze a set of 166 SAR images collected throughout the 102 day interval from 24 April 2010 to 3 August 2010 (supporting information Table S2) [*Garcia-Pineda et al.*, 2013b]. The output generated discrete estimates for the total area of oil-covered water, irrespective of thickness, within the geographic region covered by each SAR image. Estimates for the much smaller patches of thick oil and oil-water emulsion were obtained by applying the Oil Emulsion Detection Algorithm (OEDA) [*Garcia-Pineda et al.*,

Table 1. Summary Statistics for Inventory of Oil-Covered Water Detected in 176 Independent SAR Image Samples of the Gulf of Mexico[a]

| | Gulf of Mexico | | Bootstrap Results | | Estimated Annual Discharge of Natural Oil | | | |
| | | | | Fraction of Total | Lower Bound | | Upper Bound | |
Subregion (10^2 km grid)	Area (km²)	Mean Oil Cover (km²)	(%)	SD	(m³)	(bbl)	(m³)	(bbl)
Northwest	321,000	530	68%	68.45	1.69×10^4	1.06×10^5	6.55×10^4	4.12×10^5
Northeast	421,000	52.4	7%	28.11	8.87×10^2	5.58×10^3	8.82×10^3	5.54×10^4
Southwest	501,000	194	25%	46.03	5.40×10^3	3.40×10^4	2.63×10^4	1.65×10^5
Southeast	230,000	3.35	<1%	10.96	0	0	1.57×10^3	9.86×10^3
Total Gulf	1,473,000	779	100%	86.24	2.53×10^4	1.59×10^5	9.48×10^4	5.96×10^5

[a]The Gulf is gridded in 10 × 10 km cells, which were divided into four subregions along the lines of 25°N latitude and 90°W longitude. Each cell was sampled in multiple SAR images. Mean volumes for oil and oil emulsion, with standard deviations, were calculated from a bootstrap replication, with replacement, of 100,000 samplings. Annual discharge volume estimates assume that natural oil slicks of area shown and 0.1 μm thickness persist for 8–24 h, with one standard deviation added to or subtracted from the upper and lower bounds, respectively.
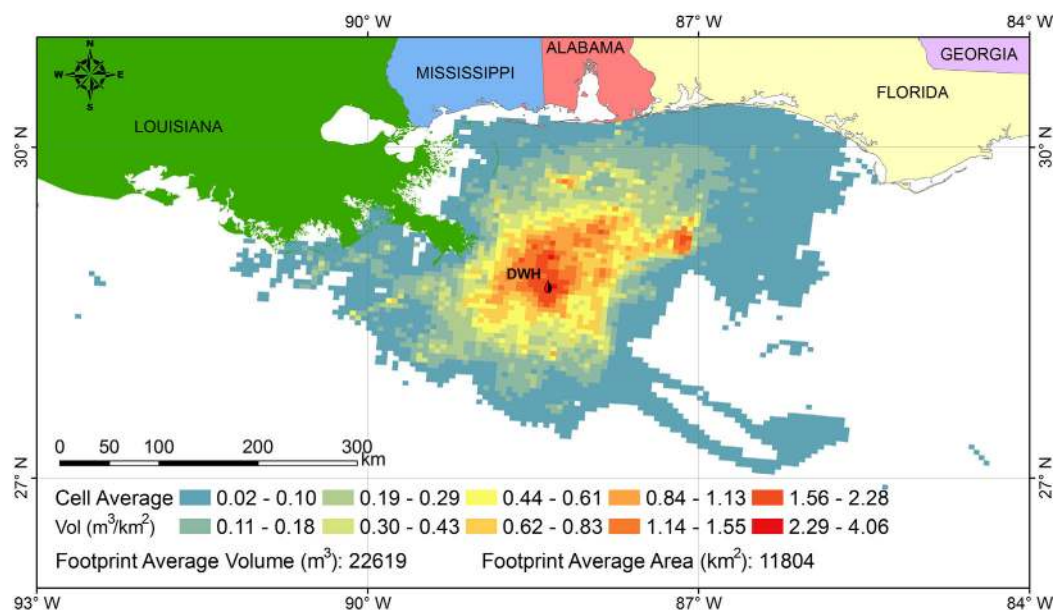
Figure 3. Map of surface oil from Deepwater Horizon: Distribution and average volume of surface oil (m^3 km^{-2}) from DWH discharge; gridded at 5×5 km scale, across a cumulative footprint of 149,000 km^2, 24 April 2010 to 3 August 2010.

2013a] to the subset of 60 SAR images in which the satellite sampled the floating oil within an incidence angle range of 19°–38° (L-band), 20°–32° (C-band), or 20°–31° (X-band). Although SAR image acquisitions were focused on the DWH area during the emergency, not all images covered the entire extent of the surface oil, and satellite overpass periods were irregular. The TCNNA or OEDA output from each SAR image was therefore treated as a statistical sample of the total surface oil. We then interpolated within the overall data to estimate the extent of the floating oil footprint in a grid of 5×5 km cells at noon and midnight UTC for the 102 days of data (Figure 3 and supporting information Database S2A).

Combining all results during the 24 April 2010 to 3 August 2010, the aggregated floating oil and oil emulsion footprints extended over an area of 149,000 km^2, from offshore Louisiana west of the Mississippi River Delta and east northeast across the DWH site to the Florida Panhandle (Figure 3). The cumulative footprint is the composite of ocean areas where floating surface oil and oil emulsion were detected during the DWH discharge. The daily footprint areas were much smaller than the cumulative area and were variable in size and location; the daily average footprint area was 11,200 km^2 (SD 8431, max 28,400 km^2). Transient events extended the cumulative footprint across a broader area of the northeast Gulf of Mexico. Examples of transient events include formation of the so-called "Tiger Tail" that resulted from entrainment of oil into the Loop Current in May [*Walker et al.*, 2011], and episodic rafting of oil onto the Mississippi, Alabama, and Florida shelf and shorelines [*Michel et al.*, 2013], which are evident in an animation of daily maps showing oil occurrence (supporting information Movie S1).

The volume of surface oil and oil emulsions at any time or location is poorly known for the DWH discharge. Quantitative airborne hyperspectral oil slick mapping [*Leifer et al.*, 2012] and UAVSAR surveillance [*Jones et al.*, 2011] by NASA showed larger areas of thin oil slicks interspersed by patches and streamers of much thicker oil and oil emulsion, a pattern repeatedly confirmed by a review of aerial imagery and responder observations [*Svejkovsky et al.*, 2012]. Technical documents used by the responders considered the thinnest oil layers to be <8 μm [*Lehr et al.*, 2010]. However, even the thinnest slicks were rarely continuous, and the thicker layers were often highly concentrated. In summarizing SAR results (see section 2), we conservatively categorized surface oil into two thickness classes: thin (average thickness ∼1 μm) and thick (average thickness ∼70 μm), with the understanding that this classification collapsed a broad spectrum of variation.

Multiplying the respective areas of thin and thick oil by these average thickness estimates and summing the results provided an estimate of the volume of surface oil and oil emulsion in each grid cell at noon and midnight (UTC) for each of the 102 days of data. A summary of the volume estimates is mapped as the average of these twice-daily interpolated values over the 102 days (Figure 3). In this figure, the minimum average surface
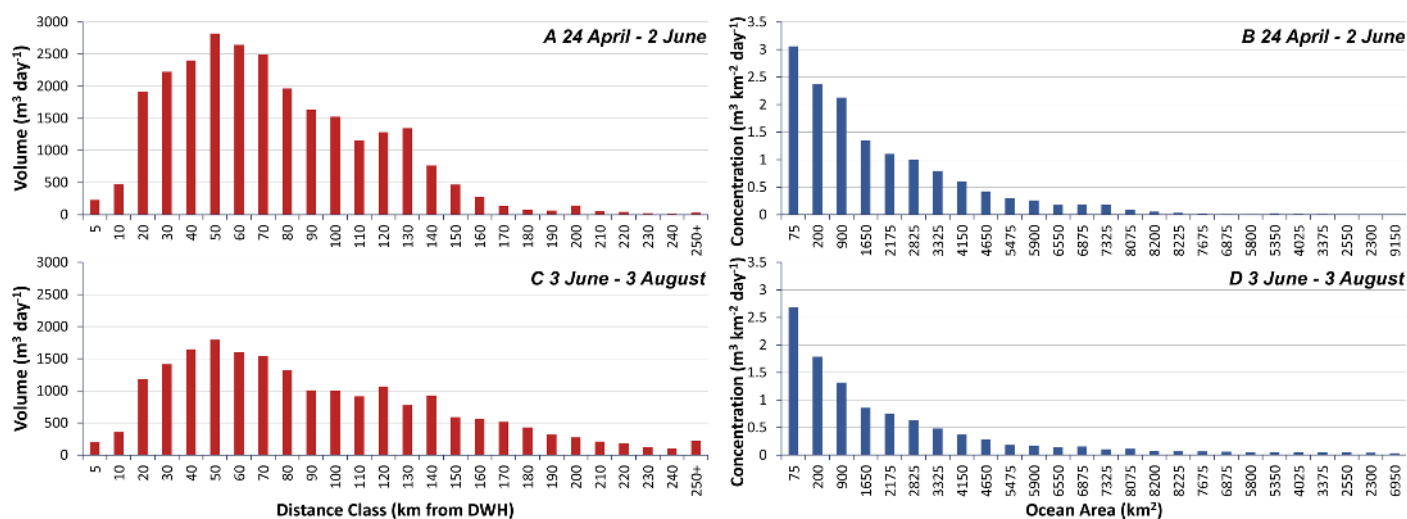
Figure 4. Surface oil magnitudes by distance from DWH: (a) Average volumes (m^3 d^{-1}) within surface oil footprint at progressive distances from the DWH accident site are shown for increments of distance 1–5, 5–10, and 20–30 km, etc. (a) Average concentrations of oil (m^3 d^{-1} km^{-2}) are shown within the increments of ocean area for distance classes in Figure 4a.

oil volume was >0.016 m^3 km^{-2}, which exceeded the maximum value for natural background oil (Figure 2). The maximum average surface oil volume for any cell over the entire 102 days was ~4 m^3 km^{-2}.

The volume of oil in a grid cell for any time period is the net sum of oil arriving at the surface, minus evaporation and other losses, lateral transport out of the cell, dispersion into the water column, and treatment by response efforts. The oil-covered area shifted constantly throughout the discharge and decreased markedly after the well was capped on 15 July. Consequently, the volume of oil in some grid cells varied greatly over time, with the amount of oil in a grid cell on a given day much larger (or smaller) than the average value for that cell across the 102 day event (Figure 3 and supporting information Movie S1). Generally, higher oil volumes were clustered in the grid cells around the DWH site, but patches of thicker oil migrated across the northeastern Gulf region and sometimes went ashore in the coastal states [*Michel et al.*, 2013].

Surface oil was generally concentrated in proximity to the DWH wreck site while discharges were ongoing (Figure 4 and supporting information Database S2B). The spatial distribution of floating oil and oil emulsion, relative to the DWH discharge point, can be expressed as its average daily volume (m^3 d^{-1}) at progressive increments of distance and as its average daily concentration (m^3 d^{-1} km^{-2}) in the geometrically increasing areas that these distance increments represent. These values include only the grid cells where oil was observed over the entire course of the discharge. The average daily volume increases out to distances of ~50 km from the well and then declines, while the average concentration steadily declines as oil is distributed over an ever increasing area. The increase in volume with distance from the DWH discharge point out to ~50 km suggests the range over which recently discharged oil surfaced and drifted across the ocean after traveling from depth. Additionally, formation of emulsion (mousse) greatly increased volume as oil weathered and traveled away from the well. Beyond 50 km, oil volume declined with further distance as oil entrainment, dispersion, and response operations removed surface oil.

The physical constraints on the discharge changed markedly during the emergency as response efforts intensified. In particular, amputation of the fallen riser pipes on 2 June 2010 focused the discharge at a single point and facilitated treatment of the discharging oil. Comparison of the average daily volumes and concentrations before and after the riser was cutoff is a way to examine the overall impact of this intervention (Figure 4). Prior to the riser amputation, the average daily volume of surface oil detected by SAR comprised a total of 26,240 m^3, with a modal distance of 50 km from the well; more than 77% of the total oil was found within 100 km from the well (Figure 4a). After riser amputation, the modal distance from the well remained 50 km, but the total average daily volume for all cells (m^3 d^{-1}) decreased to 20,310 m^3; less than 65% of the total oil was observed with 100 km from the site (Figure 4c). The approximate exponential decline in concentration of oil at greater distances was more rapid prior to the event (Figure 4b). Concentration of oil (m^3 d^{-1} km^{-2}) decreased after amputation of the riser (Figure 4d). Understanding possible underlying causes for these global differences requires examining the temporal record of the surface oil detected by SAR.
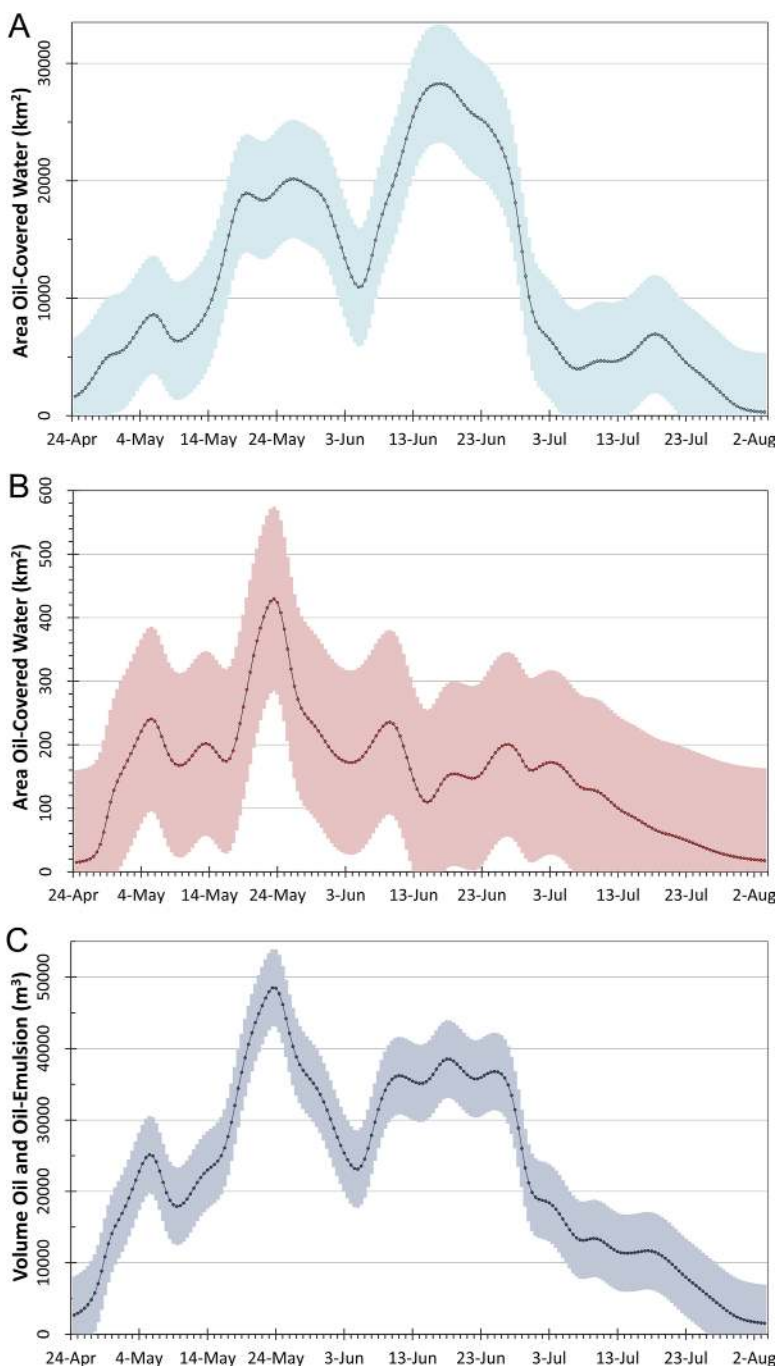
Figure 5. Time series of surface oil (area and volume) from DWH: (a) area of oil-covered water irrespective of oil thickness (km²); outline shows confidence interval (±1 SD). (b) Area of thick oil (∼70 μm) exclusively—note scale change (km²); outline shows confidence interval (±1 SD). (c) Combined volume of floating oil (m³); outline shows confidence interval (±1 SD). For a region of the same area, thick oil constitutes a volume seventyfold greater than thin oil.

3.3. Temporal Variation of DWH Surface Oil

Summing the 12 h interpolated values for the total oil footprint and the amount of thick oil across all cells in the 149,000 km² region of impact provides a record of the area and volume of surface DWH oil over the period 24 April 2010 to 3 August 2010. Results show a modulated pattern of increase and decrease in the total oil-covered area (Figure 5a and supporting information Database S2B). The greatest areal coverage of surface oil, irrespective of thickness, occurred on 23 May and 18 June; notable minor peaks occurred on about 6 May and 18 July. Exhibiting a different trend, the area covered by thick oil alone increased steadily

Table 2. Statistics of Surface Oil Variation During DWH: Summary Estimates Were Calculated for SAR Detected Oil Footprint Area and Volume During the Time Period 24 April 2010 to 3 August 2010[a]

Units	Peak Values			Summary Values		
	6 May	23 May	18 June	Average	Maximum	SD
Area (km^2)	8,500	18,900	28,100	11,800	28,200	5,028
Thick volume (m^3)	16,000	29,500	10,500	10,800	29,500	2,001
Total volume (m^3)	26,000	48,500	38,500	20,000	48,500	5,412
Total volume/area	2.90	2.57	1.37	1.80	5.04	0.4897

[a]Peak area and volume values for all surface oil occurred in May and June. Units of area, volume, and concentration are reported to three significant figures; standard deviation (no units) is reported to four significant figures.

after the sinking of DWH until 6 May, and then decreased about 25% before expanding to its maximum extent on 23 May (Figure 5b). Thereafter, the thick oil coverage declined.

Combining the areas of ~1 and ~70 μm oil thickness classes shows how the changes in total volume contrast with the changes in total area (compare Figures 5a and 5c). Between the maxima of 23 May and 18 June, the interpolated estimates for volume of surface oil decreased by 21%, while estimates of the area it covered increased by 49% (Table 2). The statistical confidence associated with the interpolation methods is presented as the standard deviation of the summary values shown in Table 2. Our conclusion is that the probabilities that ocean area covered by oil was greater on 18 June than on 23 May, while volume of the oil decreased between these same dates, were greater than 0.90. Comparison of the peak values for oil area and volume for 6 May, 23 May, and 18 June also shows the changing relative importance of the thin and thick classes during different phases of the discharge. In the initial phases up to 23 May, thick oil comprised 60% of the total volume of surface oil. The percentage of thick oil in the total volume then decreased and contributed just 27% to the 18 June peak (Table 2). A sensitivity analysis showed that utilizing a broad range of scalars in the "thick oil" thickness, from 50 to 100 μm, did not change the fundamental conclusions of this study. It is important to note that the variation in surface oil area and volume detected by SAR occurred in the context of increasing action by the responders and dynamic environmental conditions.

The cumulative effect of response actions was to reduce the rate of discharge through direct recovery and to increase the amount of discharged oil treated with dispersant and controlled burns; however, these efforts were initiated in different sequences (Figure 6). Application of Corexit® dispersant from aircraft was most aggressive in the earlier phases of the discharge, but became more measured as the response progressed [*Houma ICP Aerial Dispersant Group*, 2010; *Lehr et al.*, 2010]. Subsea application of dispersant into the buoyant plume of oil and gas, a previously untested procedure, was initiated on 5 May [*Lehr et al.*, 2010]. After the riser amputation on 2 June, dispersant applications of greater and greater quantity were
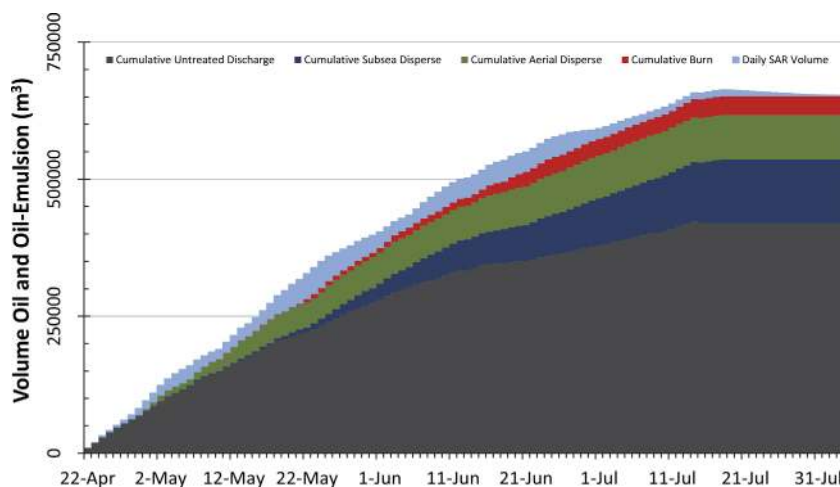

Figure 6. Cumulative discharges of untreated and treated oil as well as oil removal by direct recovery and surface burning. Values are taken from the *Lehr et al.* [2010], Appendix 3, and assume that dispersant can treat oil and ratios of 1:20 for aerial application and 1:40 for subsea applications. Daily volume of surface oil detected by SAR (m^3), taken from the present results, is plotted for comparison.
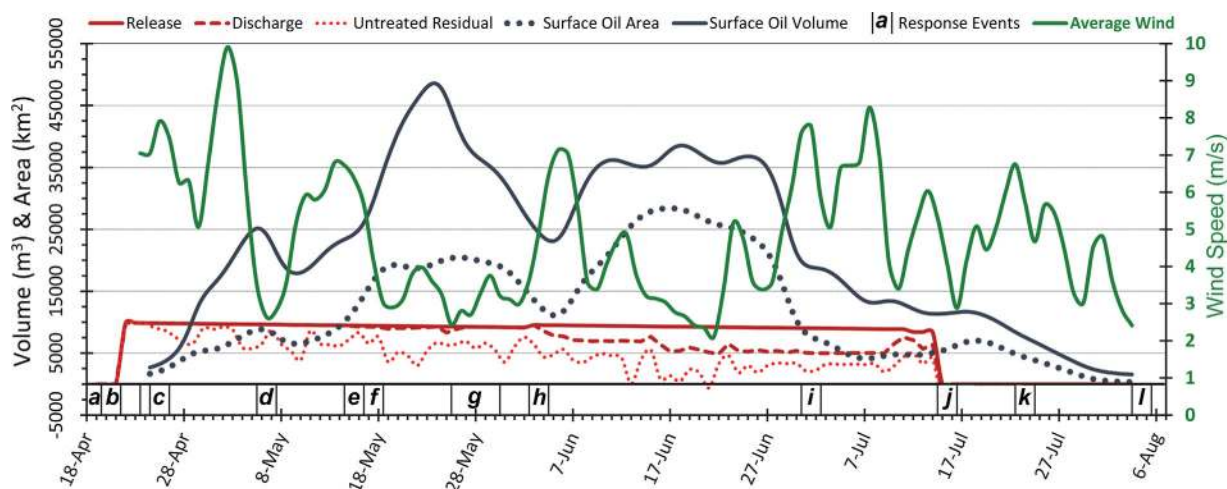
Figure 7. Time series of DWH discharge plotted with surface oil and average wind speeds. Release magnitudes show best daily estimates of oil escaping from the damaged well. Discharge subtracts the oil recovered from the gross release, while treatment further subtracts burned and dispersed by aerial and subsea applications of Corexit at maximum efficacy. Response events potentially affected spread of surface oil: (a) Macondo Well blowout occurs, (b) DWH drillship sinks and release begins, (c) aerial dispersant application begins, (d) containment dome attempt fails; burning surface oil begins (e) subsea dispersant campaign begins (5 May), (f) flaring of recovered oil begins, (g) top-kill attempt, (h) riser cut from blow-out preventer; direct injection of subsea dispersant begins, (i) Hurricane Alex makes landfall, (j) capping stack closure stops release, (k) Tropical Storm Bonnie makes landfall, and (l) well killed by static backfill.

applied with increasing focus directly into escaping oil and gas at the point of discharge. Controlled burn operations that targeted regions of thick oil on the surface increased substantially during calm weather conditions in the first 3 weeks of June [*Mabile and Allen*, 2010].

Plotting the daily volumes of surface oil seen by SAR with the cumulative volumes of untreated and treated discharge over time (Figure 6) illustrates how the surface oil present at any time reflected losses compared to the cumulative discharge due to oil that dispersed in the water column before reaching the surface and was subsequently removed by dispersion, bacterial consumption, sinking, and going ashore [*Leifer et al.*, 2012; *Reed et al.*, 1999; *Ryerson et al.*, 2011]. Without these predictable loss processes, oil would have accumulated on the surface to a degree more commensurate with the rate of discharge. However, short-term variations in surface oil area and volume were greater than what can be explained by natural losses and the combined response efforts (supporting information Movie S1). Environmental conditions played a crucial role in the ability of SAR to detect floating oil.

Wind is a primary driver of evaporation, entrainment, dispersion, and transport of surface oil [*Brekke and Solberg*, 2005; *Espedal and Wahl*, 1999; *Reed et al.*, 1999]. At wind speeds 5 m s^{-1} and above, SAR is increasingly less effective at detecting a contrast between oil-dampened surface roughness and surrounding backscatter [*Brekke and Solberg*, 2005; *Espedal and Wahl*, 1999]. The oil may still have been at or near the surface, but SAR was less able to detect it—at least until the wind subsided and surface slicks reformed. Generally, expansion of surface oil area and volume detectable to SAR occurred during periods of low wind, while peaks in average wind speed corresponded to contraction of these values (Figure 7 and supporting information Movie S1). The strongest relationship among surface oil magnitude and the other factors discussed previously was the negative correlation ($R^2 = 0.45$) between the average wind speed and surface oil area.

The peak magnitudes of surface oil observed on 23 May and 18 June corresponded to two equivalent phases of about 14 days, when wind speeds were ideal for detecting surface oil; these phases were bookended by episodes of higher winds. From late May onward, the response effort began to gain an upper hand on the discharge. Key milestones (indicated along the base of Figure 7) marked overall progress in this regard.

The surface oil was dissipated further by the high wind events associated with Hurricane Alex around 1 July in the final phase of the surface-oil time series (Figure 7). Installation and closure of the capping stack on 15 July ended discharge from the well. However, areal extent of the surface oil expanded during a brief interval of low winds around 18 July, perhaps as residual oil escaped from the wreckage, or as a result of curtailed dispersant applications during capping stack installation. Surface oil virtually disappeared from SAR detection after the high winds associated with Tropical Storm Bonnie swept through the northeastern Gulf. The

response effort at sea concluded with the static kill of the well on 4 August 2010, by which time almost no DWH oil was visible on the surface of the Gulf of Mexico.

4. Discussion and Conclusions

SAR and other satellite-based remote sensing of surface oil have provided unparalleled coverage of the Gulf of Mexico over space and time. However, estimates of volume and flux must be qualified by the fact that thickness determination using present remote sensing technology remains imprecise. Measuring oil slick thickness under marine conditions is very challenging; during the DWH spill, few attempts were made to quantify oil slick thickness using satellite-based sensors. Estimates for the thickness of oil slicks from natural discharges are based on colorimetric evaluations, but have an inherently qualitative range [*ASTM International*, 2006; *NOAA Hazmat*, 2012]. Quantitative in situ analysis of oil slick thicknesses conducted concurrently with the collection of remote sensing images has rarely occurred. In many ways, the physical oceanography of the northeastern Gulf of Mexico was markedly underobserved during one of the greatest environmental crises in U.S. history, and it remains so in the aftermath. The hypothesis we propose to explain what happened to the surface discharge of DWH oil needs testing by independent approaches such as biological and chemical tracers and physical models of surface-oil advection, weathering, and fate. Recent results that track the fallout of the subsurface plume [*Valentine et al.*, 2014] might be combined with information about the surface oil to provide additional insight on the interaction of surface and midwater fractions of the discharge.

Notwithstanding these limitations, this study offers clear distinctions between natural seeps and the DWH discharge. A persistent natural oil slick, fed by a fixed geologic process, is observed in a relatively restricted area. On the ocean surface, the slick's curvilinear form flutters away from the seafloor discharge point in a continuous, wind-driven orbit. Freshly surfacing oil constantly renews the slick's origin; then it rapidly disappears, consumed and dispersed by weathering processes, after drifting across the ocean for a few hours. This repeated pattern makes it possible to predict the location of the slick's geologic source and, with reasonable estimates of volume and time scale, to calculate a flux.

Seep sources are most common and productive in the northwestern and southwestern sectors of the Gulf, while the northeast region where DWH occurred produces comparatively little natural oil seepage. The background contribution of natural seeps in the northeastern Gulf had negligible effect on the floating oil footprint and the volume of oil and oil emulsion generated during the DWH discharge. The maximum surface oil concentration from natural seeps we found in any area was about 0.015 m^3 km^{-2}, while the daily surface oil concentration of DWH exceeded 20 m^3 km^{-2} on many occasions (supporting information Figure S3). Moreover, the minimum average concentration of DWH surface oil (Figure 3) was >0.015 m^3 km^{-2}. The two distributions do not overlap in our presentation, which is an indication of how completely the DWH oil overwhelmed background seepage during the spring and summer of 2010.

Remote sensing assessment of reduced oil thicknesses resulting from subsea dispersant application played an important role in justifying this important response action [*Lehr et al.*, 2010]. The effects of dispersant application, especially the subsea application, on formation of deep-sea oil plumes have subsequently been modeled by a number of researchers [*Paris et al.*, 2012; *Socolofsky et al.*, 2015]. Comparison of modeling results with more complete remote sensing spatial and temporal data can advance understanding in both fields.

The present study should not be taken as an absolute determination of the extent and distribution of surface oil thicknesses during the DWH discharge. Rather, we used SAR data to quantify the overall extent of surface oil, the vast majority of which occurred as thin (1 μm) layers, and the much more restricted occurrence of patches of thick (70 μm) emulsified oil. Summing these two classes yielded consistent estimates for relative changes in the spatial and temporal characteristics of the surface oil footprint. On the ocean surface, the DWH oil footprint occupied a dynamically changing region, with heaviest oil concentrated in the region ~50 km from the DWH wreck site, while thin filaments and transient patches of thick oil extended far from the source and to coastal areas. The technique of gridding oil volumes on maps and interpolating among images with partial coverage has not to our knowledge been previously used to assess oil spill impacts or natural seeps. Although fine-scale and transient details may be smoothed over with this approach, impacts

to the pelagic, benthic, and littoral ecosystems can be evaluated within a common reference framework. The data sets provided as supporting information can be the basis for future studies in diverse fields.

The surface oil detected by SAR was a blend of what had been treated with dispersant at the seafloor and on the surface plus the untreated residual. Controlled burning operations further reduced the amount of thick oil on the surface. These relative fractions changed on a daily basis, and SAR analysis cannot distinguish among them. Neither do these conditions permit an accurate calculation of DWH oil fluxes to the surface based on the SAR results. Moreover, analysis of polarimetric SAR data suggests that substantial fractions of the DWH surface oil was mixed into the upper water column as opposed to being present as a viscoelastic films [*Minchew*, 2012]. We conclude, however, that response efforts contributed to dispersing the DWH oil over a larger area, while reducing its total surface volume, until wind and other weathering processes removed it entirely from the sea surface of the Gulf of Mexico. Even when the oil was dispersed in this manner during the June phase, patches of thick oil continued to go ashore on beaches in Louisiana, Mississippi, Alabama, and Florida at distances of tens to hundreds of km from the well. These results suggest that dispersant application presents a potential tradeoff between surface volume and areal extent. An ecological cost and benefit analysis comparing the adverse effects of more widespread thin oil versus more confined thicker oil would be a useful step for evaluating future dispersant protocols as well as better models for the effects of background oil pollution from natural sources.

References

Abrams, M. A. (2005), Significance of hydrocarbon seepage relative to petroleum generation and entrapment, *Mar. Pet. Geol.*, *22*(4), 457–477.

Aeppli, C., C. M. Reddy, R. K. Nelson, M. Y. Kellermann, and D. L. Valentine (2013), Recurrent oil sheens at the deepwater horizon disaster site fingerprinted with synthetic hydrocarbon drilling fluids, *Environ. Sci. Technol.*, *47*(15), 8211–8219, doi:10.1021/es4024139.

ASTM International (2006), Standard guide for visually estimating oil spill thickness on water, in *ASTM Committee F20 on Hazardous Substances and Oil Spill Response*, p. 4, West Conshohocken, Pa.

Boehm, P. D., and P. D. Carragher (2012), Location of natural oil seep and chemical fingerprinting suggest alternative explanation for deep sea coral observations, *Proc. Natl. Acad. Sci. U. S. A.*, *109*(40), E2647, doi:10.1073/pnas.1209658109.

Brekke, C., and A. H. S. Solberg (2005), Oil spill detection by satellite remote sensing, *Remote Sens. Environ.*, *95*(1), 1–13, doi:10.1016/j.rse.2004.11.015.

Brooks, J. M., et al. (1990), Salt, seeps and symbiosis in the Gulf of Mexico, *Eos Trans. AGU*, *71*, 1772–1773.

Bryant, R. B., J. Lugo, C. Cordova, and A. Salvador (1991), Physiography and bathymetry, in *The Geology of North America, The Gulf of Mexico Basin*, edited by A. Salvador, Geol. Soc. of Am., Boulder, Colo.

Bulgarelli, B., and S. Djavidnia (2012), On MODIS retrieval of oil spill spectral properties in the marine environment, *IEEE Geosci. Remote Sens. Lett.*, *9*(3), 398–402, doi:10.1109/LGRS.2011.2169647.

Camilli, R., C. M. Reddy, D. R. Yoerger, B. A. S. Van Mooy, M. V. Jakuba, J. C. Kinsey, C. P. McIntyre, S. P. Sylva, and J. V. Maloney (2010), Tracking hydrocarbon plume transport and biodegradation at Deepwater Horizon, *Science*, *330*(6001), 201–204, doi:10.1126/science.1195223.

Chanton, J., T. Zhao, B. Rosenheim, S. B. Joye, S. Bosman, K. Yeager, A. R. Diercks, and D. Hollander (2015), Tracing of the flux of petrocarbon to the sea floor associated with the Deepwater Horizon event, *Environ. Sci. Technol.*, *49*, 847–854, doi:10.1021/es5046524.

Chernick, M. R. (1999), *Bootstrap Methods: A Practicioner's Guide*, John Wiley, N. Y.

Clark, R. N., et al. (2010), A method for quantitative mapping of thick oil spills using imaging spectroscopy, *U.S. Geol. Surv. Open File Rep., 2010-1167*, 51 pp.

Cressie, N. A. C. (1991), *Statistics for Spatial Data*, 900 pp., John Wiley, N. Y.

Crooke, E., A. Talukder, A. Ross, C. Trefry, M. Caruso, P. Carragher, C. Stalvies, and S. Armand (2015), Determination of sea-floor seepage locations in the Mississippi Canyon, *Mar. Pet. Geol.*, *59*, 129–135, doi:10.1016/j.marpetgeo.2014.08.004.

Daneshgar Asl, S., J. F. Amos, P. Woods, O. Garcia-Pineda, and I. R. MacDonald (2015), Chronic, anthropogenic hydrocarbon discharges in the Gulf of Mexico, *Deep Sea Res., Part II*, doi:10.1016/j.dsr2.2014.12.006, in press.

De Beukelaer, S. M., I. R. MacDonald, N. L. Guinnasso, and J. A. Murray (2003), Distinct side-scan sonar, RADARSAT SAR, and acoustic profiler signatures of gas and oil seeps on the Gulf of Mexico slope, *Geo Mar. Lett.*, *23*(3–4), 177–186.

Espedal, H., and T. Wahl (1999), Satellite SAR oil spill detection using wind history information, *Int. J. Remote Sens.*, *20*(1), 49–65.

Fingas, M., and B. Fieldhouse (2012), Studies on water-in-oil products from crude oils and petroleum products, *Mar. Pollut. Bull.*, *64*(2), 272–283, doi:10.1016/j.marpolbul.2011.11.019.

Garcia-Pineda, O., B. Zimmer, M. Howard, W. Pichel, X. Li, and I. R. MacDonald (2009), Using SAR images to delineate ocean oil slicks with a texture classifying neural network algorithm (TCNNA), *Can. J. Remote Sens.*, *35*(5), 411–421.

Garcia-Pineda, O., I. MacDonald, B. Zimmer, B. Shedd, and H. Roberts (2010), Remote-sensing evaluation of geophysical anomaly sites in the outer continental slope, northern Gulf of Mexico, *Deep Sea Res., Part II*, *57*(21–23), 1859–1869, doi:10.1016/j.dsr2.2010.05.005.

Garcia-Pineda, O., I. MacDonald, C. Hu, J. Svejkovsky, M. Hess, D. Dukhovskoy, and S. L. Morey (2013a), Detection of floating oil anomalies from the deepwater horizon oil spill with synthetic aperture radar, *Oceanography*, *26*(2), 124–137.

Garcia-Pineda, O., I. R. MacDonald, X. Li, C. R. Jackson, and W. G. Pichel (2013b), Oil spill mapping and measurement in the Gulf of Mexico with Textural Classifier Neural Network Algorithm (TCNNA), *IEEE J. Selec. Top. Appl. Earth Obs. Remote Sens.*, *6*, 2517–2525.

Garcia-Pineda, O. M., I. R. Macdonald, M. Silva, W. Shedd, S. Daneshgar Asl, and B. Schumaker (2015), Transience and persistence of natural hydrocarbon seepage in Mississippi canyon, Gulf of Mexico, *Deep Sea Res., Part II*, doi:10.1016/j.dsr2.2015.05.011, in press.

Hine, A. C., G. R. Brooks, R. A. Davis, D. S. Duncan, S. D. Locker, D. C. Twichell, and G. Gelfenbaum (2003), The west-central Florida inner shelf and coastal system: A geologic conceptual overview and introduction to the special issue, *Mar. Geol.*, *200*(1–4), 1–17, doi:10.1016/S0025-3227(03)00161-0.

Houma ICP Aerial Dispersant Group (2010), *After Action Report Deepwater Horizon MC252 Aerial Disperant Response*, Houma Incident Command Post, Houma, USA. [Available at http://www.mdl2179trialdocs.com/releases/release201501260800005/TREX-013037.pdf.]

Hu, C., X. Li, W. G. Pichel, and F. E. Muller-Karger (2009), Detection of natural oil slicks in the NW Gulf of Mexico using MODIS imagery, *Geophys. Res. Lett.*, *36*, L01604, doi:10.1029/2008GL036119.

Hu, C., R. H. Weisberg, Y. Liu, L. Zheng, K. L. Daly, D. C. English, J. Zhao, and G. A. Vargo (2011), Did the northeastern Gulf of Mexico become greener after the Deepwater Horizon oil spill?, *Geophys. Res. Lett.*, *38*, L09601, doi:10.1029/2011GL047184.

Janjic, Z., R. Gall, and M. Pyle (2010), Scientific documentation for the NMM Solver, *NCAR Tech. Note NCAR/TN-477+STR*, 54 pp., Natl. Cent. for Atmos. Res., Boulder, Colo., doi:10.5065/D6MW2F3Z.

Jones, C., B. Minchew, and B. Holt (2011), Polarimetric decomposition analysis of the Deepwater Horizon oil slick using L-band UAVSAR data, in *2011 IEEE International Geoscience & Remote Sensing Symposium*, pp. 2278-2281, IEEE International, N. Y.

Lehr, W., S. Bristol, and A. Possolo (2010), *Oil Budget Calculator Deepwater Horizon*, *Technical Documentation*, The Federal Interagency Solutions Group. [Available at http://www.restorethegulf.gov/sites/default/files/documents/pdf/OilBudgetCalc_Full_HQ-Print_111110.pdf.]

Leifer, I., et al. (2012), State of the art satellite and airborne marine oil spill remote sensing: Application to the BP Deepwater Horizon oil spill, *Remote Sens. Environ.*, *124*, 185–209, doi:10.1016/j.rse.2012.03.024.

Leung, T., and J. Malik (2001), Representing and recognizing the visual appearance of materials using three-dimensional textons, *Int. J. Comput. Vision*, *43*(1), 29–44.

Lubchenco, J., M. K. McNutt, G. Dreyfus, S. A. Murawski, D. M. Kennedy, P. T. Anastas, S. Chu, and T. Hunter (2012), Science in support of the Deepwater Horizon response, *Proc. Natl. Acad. Sci. U. S. A.*, *109*(50), 20,212–20,221, doi:10.1073/pnas.1204729109.

Mabile, N., and A. Allen (2010), *Controlled Burns After Action Report Burns on May 28th–August 3, 2010*, Controlled Burn Group, Houma Incident Command Post, Houma, USA. [Available at http://www.mdl2179trialdocs.com/releases/release201501260800005/TREX-241730.pdf.]

MacDonald, I. R. (2011), Remote sensing and sea-truth measurements of methane flux to the atmosphere (HYFLUX project), final report DE-NT0005638, 85 pp., Natl. Energy Technol. Lab., Dep. of Energy, Morgantown, USA.

MacDonald, I. R., N. Guinasso, S. Ackleson, J. Amos, R. Duckworth, R. Sassen, and J. Brooks (1993), Natural oil-slicks in the Gulf of Mexico visible from space, *J. Geophys. Res.*, *98*(C9), 16.351–16,364.

MacDonald, I. R., J. F. Reilly Jr., S. E. Best, R. Venkataramaiah, R. Sassen, J. Amos, and N. L. J. Guinasso (1996), A remote-sensing inventory of active oil seeps and chemosynthetic communities in the northern Gulf of Mexico, in *Hydrocarbon Migration and Its Near-Surface Expression, AAPG Mem. 66*, pp. 27–37, Am. Assoc. of Pet. Geol., Tulsa, Okla.

MacDonald, I. R., I. Leifer, R. Sassen, P. Stine, R. Mitchell, and N. Guinasso (2002), Transfer of hydrocarbons from natural seeps to the water column and atmosphere, *Geofluids*, *2*(2), 95–107.

MacDonald, I. R., W. W. Sager, and M. B. Peccini (2003), Association of gas hydrate and chemosynthetic fauna in mounded bathymetry at mid-slope hydrocarbon seeps: Northern Gulf of Mexico, *Mar. Geol.*, *198*, 133–158.

MacDonald, I. R., et al. (2004), Asphalt volcanism and chemosynthetic life, Campeche Knolls, Gulf of Mexico, *Science*, *304*, 999–1002.

MacDonald, I. R., S. Daneshgar Asl, and O. M. Garcia Pineda (2013), Surface oil drift rates estimated from natural seeps, in *2013 Gulf of Mexico Oil Spill and Ecosystem Science Conference*, New Orleans, La, Gulf of Mexico Alliance, Ocean Springs, USA.

Maianti, P., M. Rusmini, R. Tortini, G. Dalla Via, F. Frassy, A. Marchesi, F. R. Nodari, and M. Gianinetto (2014), Monitoring large oil slick dynamics with moderate resolution multispectral satellite data, *Nat. Hazards*, *73*(2), 473–492, doi:10.1007/s11069-014-1084-9.

Marghany, M. (2014), Utilization of a genetic algorithm for the automatic detection of oil spill from RADARSAT-2 SAR satellite data, *Mar. Pollut. Bull.*, *89*(1–2), 20–29, doi:10.1016/j.marpolbul.2014.10.041.

McBride, B. C., M. G. Rowan, and P. Weimer (1998), The evolution of Allochthonous salt systems, northern green canyon and ewing bank (offshore Louisiana), northern Gulf of Mexico, *AAPG Bull.*, *82*(5B), 1013–1036.

McNutt, M. K., R. Camilli, T. J. Crone, G. D. Guthrie, P. A. Hsieh, T. B. Ryerson, O. Savas, and F. Shaffer (2011), Review of flow rate estimates of the Deepwater Horizon oil spill, *Proc. Natl. Acad. Sci. U. S. A.*, *109*, 20,260–20,267, doi:10.1073/pnas.1112139108.

Michel, J., et al. (2013), Extent and degree of shoreline oiling: *Deepwater Horizon* oil spill, Gulf of Mexico, USA, *PLoS ONE*, *8*(6), e65087, doi:10.1371/journal.pone.0065087.

Minchew, B. (2012), Determining the mixing of oil and sea water using polarimetric synthetic aperture radar, *Geophys. Res. Lett.*, *39*, L16607, doi:10.1029/2012GL052304.

Miranda, F. P., A. M. Q. Marmol, E. C. Pedroso, C. H. Beisl, P. Welgan, and L. M. Morales (2004), Analysis of RADARSAT-1 data for offshore monitoring activities in the Cantarell Complex, Gulf of Mexico, using the unsupervised semivariogram textural classifier (USTC), *Can. J. Remote Sens.*, *30*(3), 424–436.

Mitchell, R., I. R. MacDonald, and K. Kvenvolden (1999), Estimates of total hydrocarbon seepage into the Gulf of Mexico based on satellite remote sensing images, *Eos Suppl.*, *80*(49), OS242.

National Research Council Committee on Oil in the Sea (2003), *Oil in the Sea III: Inputs, Fates and Effects*, 280 pp., The National Academies Press, Washington, D. C.

NOAA Hazmat (2012), Open water oil identification job aid for aerial observation, Office of Response and Restoration, Version 2. [Available at http://response.restoration.noaa.gov/sites/default/files/OWJA_2012.pdf.]

Paris, C. B., M. Le Henaff, Z. M. Aman, A. Subramaniam, J. Helgers, D.-P. Wang, V. H. Kourafalou, and A. Srinivasan (2012), Evolution of the macondo well blowout: Simulating the effects of the circulation and synthetic dispersants on the subsea oil transport, *Environ. Sci. Technol.*, *46*(24), 13,293–13,302, doi:10.1021/es303197h.

Pindell, J. L., and L. Kennan (2007), Rift models and the salt-cored marginal wedge in the northern Gulf of Mexico: Implications for deep water Paleogene Wilcox deposition and basin-wide maturation, in *Transactions of GCSSEPM 27th Annual Bob F. Perkins Research Conference*, pp. 146–186, Gulf Coast Section Society of Sedimentary Geology, Houston, USA.

Reed, M., O. Johansen, P. J. Brandvik, P. Daling, A. Lewis, R. Fiocco, D. Mackay, and R. Prentki (1999), Oil spill modeling towards the close of the 20th century: Overview of the state of the art, *Spill Sci. Technol. Bull.*, *5*(1), 3–16, doi:10.1016/s1353-2561(98)00029-2.

Roberts, H., and G. Boland (2010), Gulf of Mexico Cold Seeps: Preface, *Deep Sea Res., Part II*, *57*(21–23), 1835–1837.

Ryerson, T. B., et al. (2011), Atmospheric emissions from the Deepwater Horizon spill constrain air-water partitioning, hydrocarbon fate, and leak rate, *Geophys. Res. Lett.*, *38*, L07803, doi:10.1029/2011GL046726.

Socolofsky, S. A., et al. (2015), Intercomparison of oil spill prediction models for accidental blowout scenarios with and without subsea chemical dispersant injection, *Mar. Pollut. Bull.*, *96*(1–2), 110–126, doi:10.1016/j.marpolbul.2015.05.039.

Sun, S., C. Hu, D. Feng, G. Swayze, J. Holmes, G. Graettinger, I. MacDonald, O. Garcia Pineda, and I. Leifer (2015), Oil slick morphology derived from AVIRIS measurements of the Deepwater Horizon oil spill: Implications for spatial resolution requirements of remote sensors, *Mar. Pollut. Bull.*, doi:10.1016/j.marpolbul.2015.12.003.

Svejkovsky, J., W. Lehr, J. Muskat, G. Graettinger, and J. Mullin (2012), Operational utilization of aerial multispectral remote sensing during oil spill response: Lessons learned during the Deepwater Horizon (MC-252) spill, *Photogramm. Eng. Remote Sens.*, *78*(10), 1089–1102.

Valentine, D. L., G. B. Fisher, S. C. Bagby, R. K. Nelson, C. M. Reddy, S. P. Sylva, and M. A. Woo (2014), Fallout plume of submerged oil from Deepwater Horizon, *Proc. Natl. Acad. Sci. U. S. A.*, *111*(45), 15,906–15,911, doi:10.1073/pnas.1414873111.

Walker, N., et al. (2011), Impacts of Loop Current frontal cyclonic eddies and wind forcing on the 2010 Gulf of Mexico oil spill, in *Monitoring and Modeling the Deepwater Horizon Oil Spill: A Record-Breaking Enterprise, Geophys. Monogr. Ser.*, vol. 195, pp. 103–116, AGU, Washington, D. C.

Watkins, J. S., J. W. Ladd, R. T. Buffler, F. J. Shaub, M. H. Houston, and J. L. Worzel (1978), Occurrence and evolution of salt in deep Gulf of Mexico, in *Framework, Facies and Oil-Trapping Characteristics of the Upper Continental Margin, AAPG Stud. Geol.*, edited by A. H. Bouma, G. T. Moore, and J. M. Coleman, Am. Assoc. of Pet. Geol., Tulsa, Okla.

Whelan, J., L. Eglinton, L. Cathles III, S. Losh, and H. Roberts (2005), Surface and subsurface manifestations of gas movement through a N-S transect of the Gulf of Mexico, *Mar. Pet. Geol.*, *22*(4), 479–497.

White, H. K., et al. (2012), Impact of the Deepwater Horizon oil spill on a deep-water coral community in the Gulf of Mexico, *Proc. Natl. Acad. Sci. U. S. A.*, *109*, 20,303–20,308, doi:10.1073/pnas.1118029109.